Front. Earth Sci. 2020, 14(2): 384–400
https://doi.org/10.1007/s11707-019-0777-5

RESEARCH ARTICLE

An ultraviolet to visible scheme to estimate chromophoric dissolved organic matter absorption in a Case-2 water from remote sensing reflectance

Xia LEI[1], Jiayi PAN (✉)[2], Adam DEVLIN[2]

1 Institute of Space and Earth Information Science, The Chinese University of Hong Kong, Hong Kong, China
2 School of Geography and Environment, Jiangxi Normal University, Nanchang 330022, China

Abstract In a typical Case-2 coastal water environment (here, the Pearl River Estuary (PRE), China), chromophoric dissolved organic matter (CDOM) and suspended particulates dominate the water optical properties, and CDOM fluorescence contributes considerably to surface water reflectance. In this paper, an ultraviolet (UV) to visible scheme to retrieve CDOM absorption (a_g) is developed based on a set of *in situ* observations. First, the CDOM UV absorption and spectral slope (S_g) are derived directly from the visible remote sensing reflectance; then the S_g is extrapolated to obtain the spectrum from UV to visible spectral range. This algorithm performs well, with an overall mean absolute percent difference (*MAPD*) of ~30%, ~5% and ~6% for the estimation of a_g in 250–450 nm, S_g over 250–400 nm, and 250–700 nm, respectively. The effectiveness and stability of the algorithm is further demonstrated in capturing the distribution pattern of CDOM absorption in the PRE from satellite ocean color imagery with multiple spatial and spectral resolution, namely: the Visible Infrared Imaging Radiometer Suite (VIIRS) (750 m/Multispectral), the Ocean and Land Color Instrument (OLCI) (300 m/Multispectral), the Hyperspectral Imager for the Coastal Ocean (HICO) (100 m/Hyperspectral), and the Landsat 8 Operational Land Imager (OLI) (30 m/Multispectral). The UV to visible scheme can benefit the CDOM absorption estimation in two aspects: 1) it is free from the disturbance of suspended matter; 2) it avoids uncertainties caused by the low signal-to-noise ratio (SNR) of a_g measurements in the visible range. The algorithm is effective in revealing multiple scales of variation of CDOM absorption from ocean color observations.

Received March 2, 2019; accepted May 5, 2019

E-mail: panj@cuhk.edu.hk

Keywords Chromophoric dissolved organic matter, ocean color remote sensing, Pearl River Estuary, ultraviolet

1 Introduction

Chromophoric dissolved organic matter (CDOM) is the light-absorbing part of dissolved organic matter (DOM) in water. The absorption spectrum of CDOM under solar radiation is primarily in the ultraviolet (UV, 250–400 nm) domain, and decreases with wavelength in an exponential manner (Blough and Del Vecchio, 2002). CDOM can considerably affect the light field in the upper water column, contribute to light attenuation in the UV and visible blue range, initiate a variety of photochemical reactions, cause inorganic carbon release, and alter the microbial bioavailability of organic matter (Siegel et al., 2002; Sharpless and Blough, 2014). CDOM is an important component of the ocean biogeochemical system and a dynamic component of the global carbon cycle (Church et al., 2002; Ducklow, 2002), due to its intensive chemical and biological activities. Its absorption spectrum is now widely used as signatures and tracers of DOM composition, source, and reactivity (Loiselle et al., 2009 and 2012; Fichot and Benner, 2012; Helms et al., 2008 and 2013; Fichot et al., 2016). Furthermore, in estuaries and coastal waters, CDOM absorption usually co-varies with salinity. Variation of CDOM absorption can be used to reveal water mass mixing in near shore waters (Laane and Kramer, 1990). Interpretation and quantification of CDOM absorption in the upper water layer is therefore crucial for understanding various processes in marine environments (Wei et al., 2016). Satellite data obtained by multiple space-borne ocean color sensors provide an efficient way to investigate CDOM variations on a large scale with various spatial and temporal resolutions.

In ocean color remote sensing, CDOM is recognized as one of the major optically active constituents in water because of its strong absorptivity to solar radiation in UV-visible range (Bricaud et al., 1981), which together with chlorophyll and suspended particulates can decide the surface water reflectance. The optical properties of water are mainly specified by plankton microorganisms in open oceans (defined as Case 1 water), where CDOM and suspended particulates are the associates whose absorptions are expected to co-vary with chlorophyll concentrations (Morel and Prieur, 1977; Morel and Gentili, 1993). In coastal and inland waters (defined as Case-2 water), the main source of CDOM and suspended matter is terrigenous input (Stedmon and Nelson, 2015). Therefore, the concentrations of CDOM and suspended non-algal particulates change independently of chlorophyll. In such cases, more unknown variables appear in remote sensing retrieval algorithms, significantly increasing uncertainties in deriving CDOM absorption from satellite data.

The Pearl River is China's second largest river in terms of discharge, delivering more than 87 million tons of suspended particulates (dominated by mineral particles) and 30 million tons of dissolved matter into the northern South China Sea every year (Chen et al., 2003). The optical properties of the estuarine water are strongly influenced by river discharge, especially during the wet season (Chen et al., 2004). Previous observations in the Pearl River Estuary (PRE) found that the annual average chlorophyll concentration is typically lower than 5 mg/m^3, while the concentration of suspended mineral particles can reach 50–100 mg/L during flood season. As a result, the average level of a_{ph} (440) (the absorption coefficient of phytoplankton at 440 nm) is usually lower than 0.1 m^{-1}, whereas a_d (440) (the absorption coefficient of suspended mineral particles at 440 nm) can be larger than 0.5 m^{-1}, reaching 1 m^{-1} in wet season at some locations. The average level of a_g(440) (the absorption coefficient of CDOM at 440 nm) is also much larger than a_{ph} (440), with an average value of 0.3–0.5 m^{-1} [18–28] (Chen et al., 2003 and 2004; Xu et al., 2004; Hong et al., 2005; Wang et al., 2007 and 2014; Yang and Chen, 2007; Zhou et al., 2007; Liu et al., 2009 and 2010; Fu et al., 2016). Under such circumstances, chlorophyll is no longer a key component to determine the above-water radiance. Instead, the suspended solids and CDOM from terrestrial input become the dominant factors affecting water color in the PRE.

The absorption spectra of CDOM and suspended mineral particles are similar; both decrease exponentially with increasing wavelength. This means it can be challenging to discriminate them when retrieving CDOM absorption using semi-analytical algorithms (IOCCG, 2016). In the open oceans where the absorption of CDOM is much higher than that of suspended particulates, it is adequate to not separate the two spectra. But for Case-2 waters such as the PRE where the absorption of CDOM and suspended solids are comparable, eliminating the influence of suspended matter is a critical step to obtain accurate CDOM absorption from the remote sensing reflectance.

One characteristic that distinguishes CDOM from suspended particulates is fluorescence. A fraction of the organic compounds in CDOM will emit radiation in the range of 300–600 nm when excited by solar radiation with a wavelength range of 240–400 nm (Stedmon and Nelson, 2015). In CDOM-abundant water bodies, fluorescence must be taken into consideration to achieve closure of semi-analytical models (Mobley, 1994). Previous studies reported a positive correlation between DOC concentration and CDOM fluorescence emission in the PRE water (Callahan et al., 2004), and three distinct principal types of fluorophores are observed: tryptophan-like (T), UV humic-like (A), and visible-terrestrial humic-like (C) fluorophores (Hong et al., 2005). Thus, in the PRE, it is reasonable to assume that part of the water-leaving radiation in the visible range can be attributed to CDOM fluorescence, which is excited by absorbed energy in the UV band. This can be considered as a theoretical base for the retrieval of CDOM absorption in the UV domain from remote sensing reflectance in the visible range.

This study explores the feasibility of retrieving CDOM absorption coefficients and spectral slopes in the UV domain from the above-water remote sensing reflectance in the visible range, and the entire spectra curve is obtained by extrapolating the CDOM absorption from UV to visible range. This method is validated against *in situ* observations using a data set collected in a previous cruise survey in the PRE during the wet season. This UV to visible scheme is expected to avoid the influence of suspended particulates, providing a useful approach to estimate CDOM absorption in the UV-visible range for Case-2 waters where suspended particulates and CDOM equally dominate the water optics. The capability of the algorithm to address CDOM absorption variations in the PRE is further tested on several ocean color satellite images with multiple spatial and spectral resolutions.

2 Data and methods

2.1 *In situ* data set

The Pearl River Estuary is located on the southern coast of Guangdong, China (22°N–22.75°N, 113.5°N–114°N), adjacent to the Northern South China Sea (NSCS). Its major branch, the Lingdingyang, has a trumpet-like shape, with four gates on the west side of the upper estuary, discharging freshwater of 6.83 × 10^{10} m^3 into the NSCS every year (Deng et al., 2015). The wet season is from April to September, with a maximum water discharge of 20000 m^3/s (Chen et al., 2004; Pan and Gu, 2016). A cruise was carried out in May, 2014, during which above-water radiometric measurements were conducted to calculate

water surface reflectance (Fig. 1(b)). At the same time, water samples were collected, filtered, and stored. Concentrations of Chlorophyll-a (Chl-a), suspended particulate matter (SPM), and the absorption coefficient of CDOM were measured in the laboratory (please refer to Lei et al. (2018) for detailed information about the laboratory analysis of Chl-a and SPM).

1) CDOM absorption

Water samples were collected from the water surface with a sampling depth of 0–1 m and were filtered with 0.2 μm Millipore polycarbonate filters and stored in the dark at 4°C. CDOM absorbance (A (λ)) was measured in a 10-cm cuvette using a Shimadzu UV-2550 spectrophotometer in the wavelength range of 190–900 nm with spectral resolution of 0.25 nm. The absorption coefficient (a_g (λ)) is calculated at 1 nm intervals for the range of 250–900 nm according to Eq. (1):

$$a_g(\lambda) = 2.303\mathrm{A}(\lambda)/L, \quad (1)$$

where L is the optical path length (here 0.1 m). An extrapolation strategy (Eq. (2)) is used to correct the scattering by residual particles in filtered samples if a_g (700) is larger than 0 (Bricaud et al., 1981).

$$a_{g\_corr}(\lambda) = a_g(\lambda) - a_g(700)(\lambda/700). \quad (2)$$

Spectral slopes (S_g) in the UV range (250–400 nm, S_g (250–400)) and the UV-visible range (250–700 nm, S_g (250–700)) are calculated by fitting the absorption spectra to an exponential model (Eq. (3)) and applying a nonlinear regression technique. The reference wavelength (λ_0) is set as 290 nm for both spectral ranges.

$$a_g(\lambda) = a_g(\lambda_0)\exp[-S_g(\lambda - \lambda_0)]. \quad (3)$$

2) Remote sensing reflectance

The upward reflected radiance by a Lambertian reflector (i.e., a Spectralon gray plaque with approximately 30% nominal reflectance) (L_p), the water surface radiance (L_{sw}) and the sky radiance (L_{sky}) in the wavelength range of 380–1000 nm were measured in sequence using a OceanOptics 4000 spectrometer, based on the methodology of "uncalibrated radiance and reflectance plaque measurements" (Mueller et al., 2002). The water surface and sky radiance

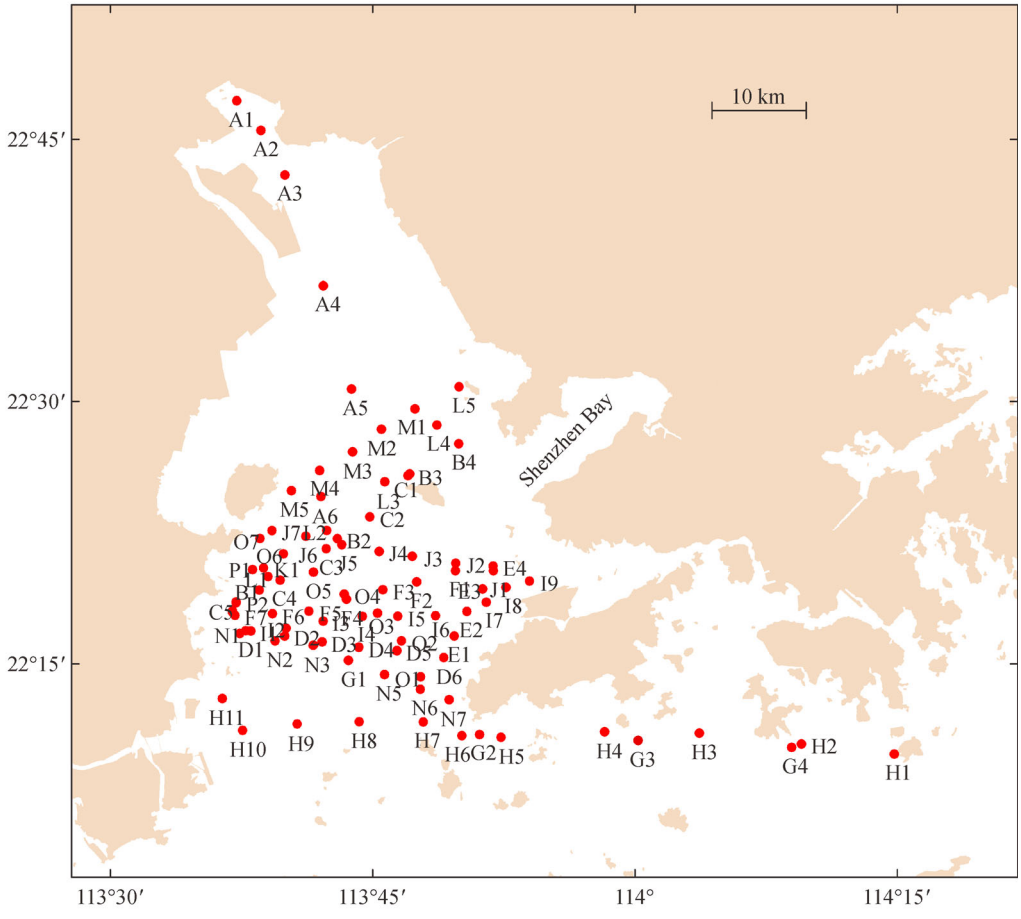

Fig. 1 Location of the stations of the Pearl River Estuary (PRE) for water surface reflectance measurements and water samples collection from a cruise in May, 2014.

were measured at a viewing angle of $(\theta, \varphi) = (40°, 135°)$ to avoid sun glint contamination and non-uniform sky radiance ((Mobley, 1999), θ is the zenith angle, φ is the azimuth angle from the solar plane). Each group of measurements was repeated 3 times.

The above-water remote sensing reflectance (R_{rs}) is defined as the ratio of water-leaving radiance (L_w) to downward irradiance just above the surface (E_d (0^+)) (Carder and Steward, 1985; Lee et al., 1994):

$$R_{rs} = \frac{L_w}{E_d(0^+)}. \tag{4}$$

The measured water surface radiance (L_{sw}) consists of water-leaving radiance (L_w) and the sky radiance (L_{sky}) reflected by air-water interface. Therefore, L_w can be calculated by:

$$L_w = L_{sw} - r_{sky} \times L_{sky}, \tag{5}$$

where r_{sky} is the sea surface reflectance factor, a function of viewing geometry, wavelength, the detector field of view (FOV), wind speed, and sky radiance distribution (Mobley, 1999). The sky conditions during the cruise were mainly overcast with a wind speed of 5–10 m/s, so r_{sky} is set as 0.0264, and the wavelength dependence is neglected based on simulation results in (Mobley, 1999).

The downward irradiance just above the surface (E_d (0^+)) is calculated according to Eq. (6):

$$E_d(0^+) = \pi L_P / \rho_P, \tag{6}$$

where ρ_p is the irradiance reflectance of the gray plaque.

The remote sensing reflectance R_{rs} is finally calculated by Eq. (7):

$$R_{rs} = \rho_p \frac{L_{sw} - r_{sky} \times L_{sky}}{L_p \times \pi}. \tag{7}$$

The remote sensing reflectance determined by any above-water methods must be converted to the exact normalized remote sensing reflectance (R_{rs}^{ex}), otherwise it is not comparable for different days or viewing angles (Mueller et al., 2002). R_{rs}^{ex} is defined as:

$$R_{rs}^{ex}(\lambda) \equiv \frac{L_{wn}^{ex}(\lambda)}{\overline{F_0}(\lambda)}, \tag{8}$$

where $\overline{F_0}(\lambda)$ is mean solar irradiance above the atmosphere at the mean sun-earth distance (d_0), $L_{wn}^{ex}(\lambda)$ is the exact normalized water-leaving radiance, which is the vertically upward radiance originating from nadir and measured with a zenith view when the sun is at zenith, without any atmospheric influence, and the earth is at its mean distance from the sun (Morel and Mueller, 2002). $L_{wn}^{ex}(\lambda)$ is related to the field measured water-leaving radiance using the above-water method by the following equation (Morel and Mueller, 2002):

$$L_{wn}^{ex}(\lambda) = \frac{L_w[\lambda, \theta, \phi, \theta_0, \tau_a, W, IOP]}{t(\lambda, \theta_0)\cos\theta_0 \left(\frac{d_0}{d}\right)^2} \frac{\mathcal{R}_0}{\mathcal{R}(\theta', W)} \frac{f_0(\lambda, \tau_a, IOP)}{Q_0(\lambda, \tau_a, IOP)} \left[\frac{f(\lambda, \theta_0, \tau_a, IOP)}{Q(\lambda, \theta', \phi, \theta_0, \tau_a, IOP)}\right]^{-1}, \tag{9}$$

where θ, ϕ are the zenith and azimuth angle for above-water radiances, θ_0 is the solar zenith angle, θ is the nadir angle for the in-water upward radiances (the Snell angle of θ), τ_a is the aerosol optical thickness, W is the wind speed, $t(\lambda, \theta_0)$ is the diffuse transmittance of the atmosphere, and d_0 and d are the mean and actual sun-earth distances, respectively. *IOPs* are the inherent optical properties including absorption and backscattering. $\mathcal{R}(\theta', W)$ represents all the reflective and refractive variations at the water-air interface, and $\mathcal{R}_0$ is $\mathcal{R}(\theta' = 0, W)$ with a constant value of 0.529. The f term is a scale factor to relate irradiance reflectance to *IOPs*, and Q is a bi-directional parameter that converts the in-water radiance into irradiance. The f_0 and Q_0 are $f(\theta_0 = 0)$ and $Q((\theta', \phi, \theta_0) = 0)$.

Both sides of Eq. (9) are divided by $\overline{F_0}(\lambda)$, yielding:

$$\frac{L_{wn}^{ex}(\lambda)}{\overline{F_0}(\lambda)} = \frac{L_w[\lambda, \theta, \phi, \theta_0, \tau_a, W, IOP]}{\overline{F_0}(\lambda)t(\lambda, \theta_0)\cos\theta_0 \left(\frac{d_0}{d}\right)^2} \frac{\mathcal{R}_0}{\mathcal{R}(\theta', W)} \frac{f_0(\lambda, \tau_a, IOP)}{Q_0(\lambda, \tau_a, IOP)} \left[\frac{f(\lambda, \theta_0, \tau_a, IOP)}{Q(\lambda, \theta', \phi, \theta_0, \tau_a, IOP)}\right]^{-1}. \tag{10}$$

Using $E_d(0^+, \lambda) = \overline{F_0}(\lambda)t(\lambda, \theta_0)\cos\theta_0(d_0/d)^2$, Eq. (8) and Eq. (4), we have:

$$R_{rs}^{ex}(\lambda) = R_{rs}(\lambda) \frac{\mathcal{R}_0}{\mathcal{R}(\theta', W)} \frac{f_0(\lambda, \tau_a, IOP)}{Q_0(\lambda, \tau_a, IOP)} \left[\frac{f(\lambda, \theta_0, \tau_a, IOP)}{Q(\lambda, \theta', \phi, \theta_0, \tau_a, IOP)}\right]^{-1}. \tag{11}$$

By using Eq. (11), the normalized reflectance (R_{rs}^{ex}) can be derived from field-measured above-water remote sensing reflectance (R_{rs}). With the viewing angles of $(\theta, \varphi) = (40°, 135°)$, namely $(\theta', \varphi) = (29°, 135°)$, and an overcast sky, the values of $\mathcal{R}$, $\mathcal{R}_0$, f_0/Q_0 and f/Q in typical coastal waters were suggested in Morel and Gentili (1993), Loisel and Morel (2001) and Morel and Mueller (2002). According to simulation results, f_0/Q_0 and f/Q are both in the range of 0.08–0.09 under overcast sky conditions, and $\mathcal{R}$ and $\mathcal{R}_0$ are 0.515–0.526 (taking an average value of 0.52) and 0.529, respectively for $(\theta, \varphi) = (40°, 135°)$. With these values, however, $R_{rs}^{ex}(\lambda)$ does not have much difference from the measured $R_{rs}(\lambda)$. Nevertheless, this

process should not be ignored or omitted if the above-water remote sensing reflectance measured under different environmental conditions are to be compared.

2.2 Satellite imagery and preprocessing

Satellite data obtained by four ocean color sensors are used for remote sensing validation of our algorithm. These sensors are the Visible Infrared Imaging Radiometer Suite (VIIRS) on board Suomi National Polar-orbiting Partnership (Suomi NPP), the Ocean and Land Color Instrument (OLCI) on board Sentinel-3A (S3A), the Hyperspectral Imager for the Coastal Ocean (HICO) integrated in the International Space Station (ISS) Window Observational Research Facility (WORF), and the Operational Land Imager (OLI) on board Landsat 8 (LS8) (Table 1). All these sensors have a spatial resolution better than 1 km. The PRE covers an area less than 2000 km^2, so these sensors are better choices as compared with the lower-resolution MODIS and SeaWiFS. Daily Level-2 products by VIIRS distributed as surface reflectance from January 2012 are available from NASA's Earth Science Data System (Vermote, 2016). Level-1B data by OLCI distributed as radiance from October 2016 are downloaded from NASA's Ocean Color Web (NASA, 2018). Level-1B products by HICO distributed as scaled and calibrated top-of-the-atmosphere (TOA) radiance from September 2009 to September 2014 can be accessed from the Oregon State University website. Level-1B data by OLI distributed as digital number (DN) from February 2013 can be downloaded from the US Geological Survey website and processed to Level-2 surface reflectance products by requesting from USGS Earth Resources Observation and Science (EROS) Center Science Processing Architecture (ESPA).

Images with cloud coverage below 20% in the study area (22°N and 23°N, 113.5°E and 114.5°E) are downloaded. The Level-1B data by OLCI are processed by the Case-2 Regional/Coastal Color (C2RCC) module in Sentinel Application Platform (SNAP) to correct atmospheric effect and calculate normalized surface reflectance. The Level-1B images from HICO are processed by the Fast Line-of-sight Atmospheric Analysis of Hypercubes (FLAASH) module in ENVI 5.2 for atmospheric correction and surface reflectance calculation. All images with non-normalized surface reflectance are normalized according to Eq. (11). VIIRS, OLCI, and HICO data are geometrically corrected by using ENVI 5.2 with the ground control points (GCPs) selected from Google Earth to obtain precise geolocation information. Water area is extracted by a reflectance threshold at the near-infrared (NIR) band. The value of the threshold is set as 10%, 15% or 20%, depending on each image. To further remove the atmospheric and water surface effects, a NIR black pixel assumption (Gordon and Wang, 1994) is applied near the open ocean area to estimate a general atmospheric scattering in the estuary, which is then extrapolated and extracted from the visible reflectance. Finally, pixels with negative reflectance values at visible bands are removed to avoid outliers.

2.3 Statistics

The accuracy of CDOM absorption and spectral slopes estimated by the new algorithm is evaluated using three statistical quantities: mean absolute percent difference (*MAPD*, Eq. (12)), root mean square error (*RMSE*, Eq. (13)) and the determination coefficient (R^2).

$$MAPD = \left[\sum |(C_{\mathrm{alg}} - C_{insitu})|/C_{insitu}\right] \times \frac{100}{N}, \quad (12)$$

$$RMSE = [\sum \ (C_{\mathrm{alg}} - C_{insitu})^2/N]^{1/2}, \quad (13)$$

where C_{alg} and C_{insitu} are the estimated and measured values of a parameter. N is the number of samples.

The observations are limited, therefore, validation of the developed algorithm is conducted using the K-fold cross validation strategy (Geisser, 1993). The mean value of the statistical indicators from cross validations is used to validate the performance of the algorithm. All statistical analysis is implemented using Matlab, version R2010a.

Table 1 The properties of ocean color remote sensors utilized in this paper. Key: VIIRS, Visible Infrared Imaging Radiometer Suite; SNPP, Suomi National Polar-orbiting Partnership; OLCI, Ocean and Land Color Instrument; HICO, Hyperspectral Imager for the Coastal Ocean; ISS, International Space Station; OLI, Operational Land Imager

Sensor	VIIRS	OLCI	HICO	OLI
Location	SNPP	Sentinel-3	ISS	Landsat 8
Data period	2010.1–Now	2016.10–Now	2009.9–2014.9	2013.2–Now
Number of bands	22	21	128	9
Spectral ranges/nm	402–12490	400–1020	353–1080	435–2294
Spatial resolution/m	375/750/1000	300	100	15/30
Revisit days	1	~2	~10	16

3 Results

3.1 *In situ* observations

Figure 2 shows the spectra of the normalized above-water remote sensing reflectance calculated by Eq. (7) and Eq. (11). The most remarkable characteristic of the spectra is the peak near 570–580 nm. The trough near 675 nm and the peak at 690–710 nm, which usually represent the absorption and fluorescence of chlorophyll, are not significant here. This is consistent with the sampling results (Fig. 3), which show a relatively low and homogenous Chl-a concentration, but apparently heterogeneous SPM concentration and CDOM absorption in the PRE during the cruise.

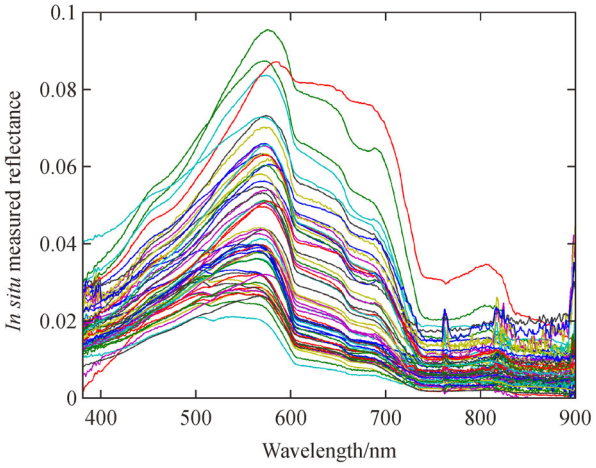

Fig. 2 Normalized *in situ* water surface reflectance at 380–900 nm measured by an Ocean Optics 4000 spectrometer using the above-water method.

To further compare the absorption level of the three components (Chl-a, CDOM, and SPM), the measured concentrations of Chl-a and SPM are converted into absorption coefficients based on the relationships given by Eqs. (14)–(17) developed by previous studies in the PRE in the same season of the year (Xu et al., 2004; Wang et al.,2007):

$$a_{\mathrm{ph}}(\lambda) = a^{*}_{\mathrm{ph}}(\lambda) \times [CHL], \tag{14}$$

$$a^{*}_{\mathrm{ph}}(\lambda) = \mathrm{A}(\lambda)[CHL]^{-\mathrm{B}(\lambda)}, \tag{15}$$

$$a_{\mathrm{d}}(\lambda) = a_{\mathrm{d}}(440)\exp(-S_{\mathrm{d}}(\lambda-\lambda_0)), \tag{16}$$

$$a_{\mathrm{d}}(440) = 0.0386SPM + 0.0048, \tag{17}$$

where a_{ph} and a_{d} are the absorption coefficients of phytoplankton and suspended detritus, respectively; a^{*}_{ph} is the specific absorption coefficient of phytoplankton; $[CHL]$ and SPM are concentrations of Chl-a and SPM, in units of mg/m^3 and mg/L, respectively; and S_{d} is the spectral slope of a_{d}. Parameters A(λ) and B(λ) in Eq. (15) are quoted from Xu et al., 2004. S_{d} in Eq. (16) is set as 0.0103 according to (Wang et al., 2007).

The calculated absorption spectra of phytoplankton and suspended matter, the measured CDOM absorption, and the comparison of the averaged spectra in 400–900 nm are displayed in Fig. 4. It is revealed by Fig. 4(d) that in the PRE during spring, the absorptions of the CDOM and the suspended matter are comparable in the visible range, and tend to jointly contribute to the low level of reflectance below 550 nm. The phytoplankton exhibits much weaker absorption over the entire wavelength range than the other two parameters. The sharp decrease of the absorption of CDOM and particulates and the occurrence of CDOM fluorescence and particle scattering can give rise to a reflectance peak near 570–580 nm (Fig. 2). The reflectance decreases dramatically for longer wavelengths (>600 nm), and drops to a low level above 700 nm because of the high absorption of pure water, but does not reach zero for most sampling stations, which is usually the case for estuarine and coastal water.

Figure 5(a) shows the correlation coefficients determined between the measured remote sensing reflectance at 380–900 nm and CDOM absorption at 250–900 nm. The strongest correlation occurs between R_{rs} at 520–670 nm and a_{g} at 250–370 nm, with correlation coefficients of 0.8 and above. In other words, it is a_{g} in the UV range, rather than the visible range, that mainly influences the visible R_{rs}. The correlation of R_{rs} and $a_{\mathrm{g}}(290)$ (CDOM absorption at 290 nm) is even more significant than that between R_{rs} and SPM concentration (Fig. 5(b)). One possible reason for this relationship is due to the emission of CDOM fluorescence in the PRE waters over a broad visible domain, which is excited by the CDOM absorbed energy in the UV range. This is evidenced by the previously reported positive correlation between DOC concentration and CDOM fluorescence emission integrated from 350 to 650 nm, which is excited by 330–340 nm in the PRE waters (Callahan et al., 2004). Although the suspended matter shows comparable absorption with CDOM in the visible range, its correlation with R_{rs} is much lower than $a_{\mathrm{g}}(290)$. The relationship between Chl-a concentration and R_{rs} is the weakest among the three components, which was expected.

3.2 Algorithm development

1) R_{rs} and $a_{\mathrm{g}}(290)$

The strongest correlation in Fig. 5(a) occurs between $R_{\mathrm{rs}}(596)$ and $a_{\mathrm{g}}(290)$, with a correlation coefficient of 0.86. Figure 6(a) shows the linear relationship between $R_{\mathrm{rs}}(596)$ and $a_{\mathrm{g}}(290)$ with the determination coefficient of 0.74. An empirical relationship Eq. (18) is therefore developed to relate $a_{\mathrm{g}}(290)$ to $R_{\mathrm{rs}}(596)$.

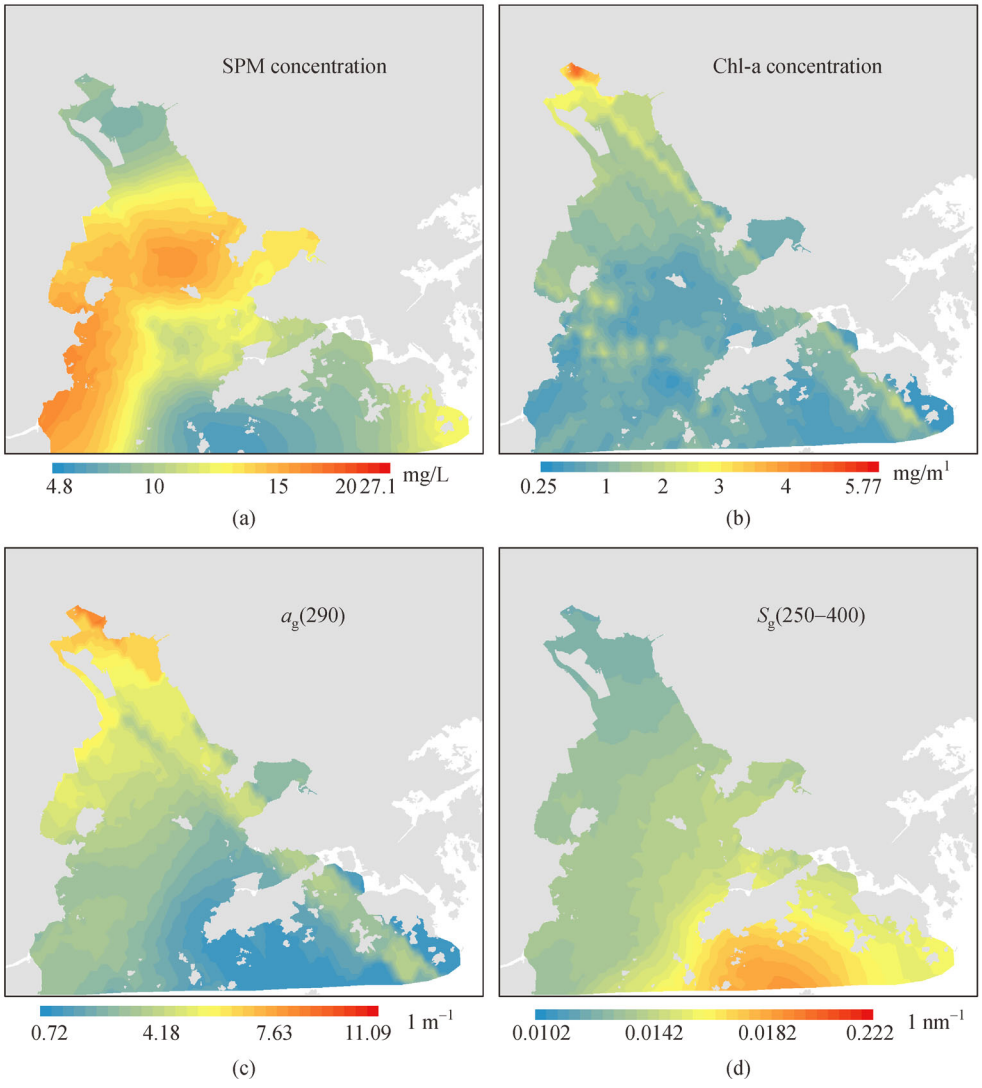

Fig. 3 Spatial distribution of (a) concentration of suspended matter (SPM, in units of mg/L); (b) concentration of chlorophyll-a (Chl-a, in units of mg/m^3); (c) CDOM absorption at 290 nm (a_g(290), in units of m^{-1}); and (d) spectral slope of CDOM absorption over 250–400 nm (S_g(250–400), in units of nm^{-1}). All figures are mapped using the Kriging interpolation method based on the discrete sampling data.

$$a_g(290) = 108.2R_{rs}(596) - 0.5324. \quad (18)$$

Since R_{rs} yields the strongest correlation with a_g(290) at 520–670 nm (Fig. 5(b)), it is advantageous to use all reflectance values over the 520–670 nm range to derive a_g(290). A principal component analysis (PCA) is an effective approach to simultaneously reduce data redundancy and maintain data variance. Results of PCA show that the normalized first principal component (PC1) explains 98.5% of the total variance of R_{rs} in 520–670 nm. Its eigenvalue is much larger than that of the rest of the components, indicating that one component is sufficient to reproduce most variance of the original reflectance in 520–670 nm, and therefore can be regarded as an effective representation of R_{rs}(520–670). Figure 6(b) shows the relationship between PC1 and a_g(290) with a correlation coefficient of 0.85, yielding another empirical algorithm (Eq. (19), denoted as "the PCA algorithm") to estimate a_g(290) from the visible R_{rs}. The determination coefficient of the PCA algorithm is 0.72, a similar performance to the R_{rs}(596) algorithm. Compared with Eq. (18), Eq. (19) is expected to be more suitable for the hyperspectral satellite data such as HICO, which has a spectral resolution as fine as 4–5 nm.

$$a_g(290) = 9.888PC1(R_{rs}(520-670)) + 3.082. \quad (19)$$

2) R_{rs} gradient and S_g(250–400)

The increase of R_{rs} from 400 to 580 nm (Fig. 2.) is mainly attributed to the decrease of absorption of CDOM and suspended matter, and the increase of CDOM fluorescence. It is found that the emission maximum of CDOM fluorescence gradually increases with increasing excitation wavelength (Stedmon and Nelson, 2015). An

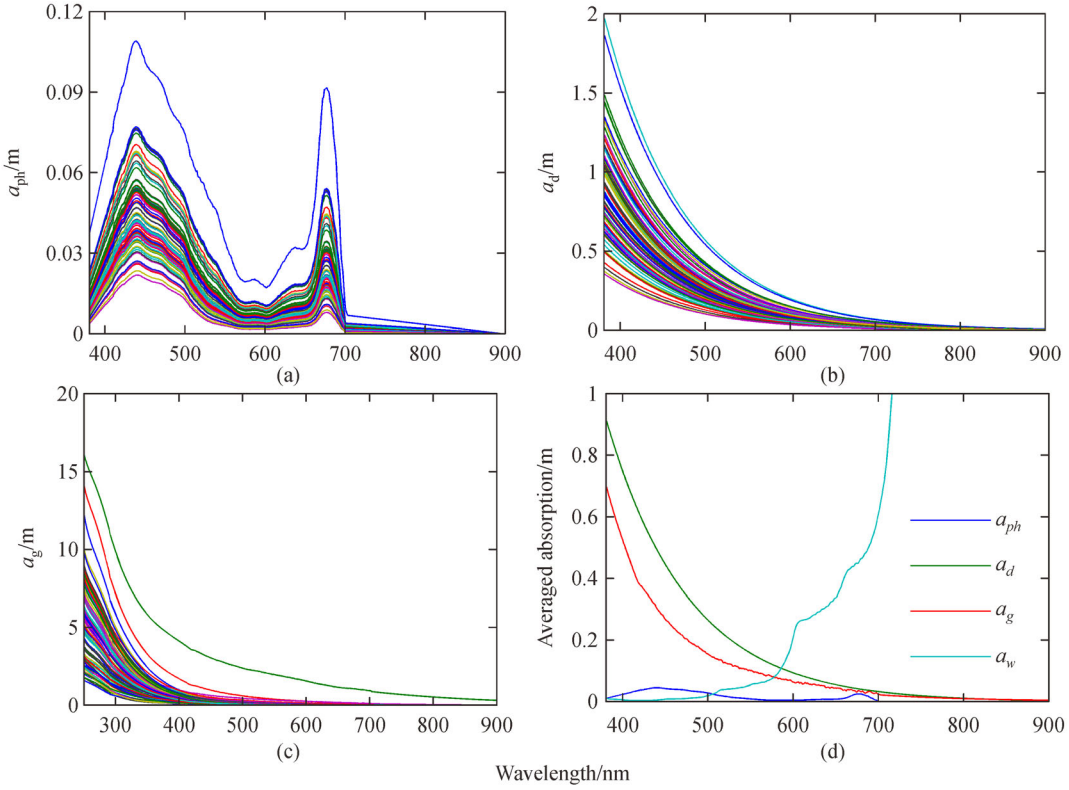

Fig. 4 Spectra of the absorption coefficients of (a) phytoplankton (a_{ph}, derived from the concentration of chlorophyll-a); (b) suspended matter (a_d, derived from the concentration of suspended matter); (c) CDOM (a_g, measured in laboratory); and (d) the comparison of the averaged a_{ph}, a_d, a_g and a_w (the absorption of pure water).

excitation wavelength increase is associated with absorption wavelength increase, and therefore a decrease of spectral slope. Since the excitation radiation for CDOM fluorescence is limited to UV domain and the emission range can extend to 600 nm, this mechanism relates the variation of S_g in the UV range to the variation of the gradient of R_{rs} in the visible domain. This connection is further evidenced by the negative correlation between the R_{rs} gradient and S_g(250–400) for the observations in the PRE (Fig. 6(c)), with a correlation coefficient of 0.73. The R_{rs} gradient here is defined as the increase rate of R_{rs} from the visible blue band to the spectral maximum, and parameterized as the average increase of R_{rs} per μm from the lower end of the visible blue band to the maximum (Eq. (20)). For the measured R_{rs} in the PRE, the wavelength of the lower end is set as 420 nm to avoid the signal noise at 380–420 nm, and the maximum R_{rs} is searched in the range of 420–700 nm, generally near 580 nm. Therefore, Eq. (21) provides a relationship to derive S_g in the UV range from the R_{rs} gradient in the visible range with a determination coefficient is 0.5296.

$$R_{rs\_Gradient} = [R_{rs_{(max)}} - R_{rs_{(min)}}]/[\lambda_{(max)} - \lambda_{(min)}], \quad (20)$$

$$S_g(250-400) = 0.01187 R_{rs\_Gradient}^{-0.1741}. \quad (21)$$

3) S_g(250–400) and S_g(250–700)

The correlation between S_g(250–400) and S_g(250–700) is strong(Fig. 6(d)). This is possibly because of the low level of CDOM absorption above 500 nm, which is close to the detection threshold of the spectrophotometer (0.046 m^{-1}). A nonlinear regression can generate a better fit to the observed CDOM absorption spectrum by preferentially weighting the higher absorption region, which reduces the influence of the a_g of low signal-to-noise ratio (SNR) at longer wavelengths on S_g estimation (Stedmon and Markager, 2001). Therefore, if the lower limit of the spectral range for S_g estimation remains the same (here, 250 nm), the estimated S_g will not change very much with a different upper wavelength limit (here, 400 and 700 nm) (Stedmon and Nelson, 2015). Nevertheless, S_g(250–700) can be extrapolated from S_g(250–400) by Eq. (22) with a correlation coefficient of 0.98.

$$S_g(250-700) = 0.0169 \times \log(S_g(250-400)) + 0.0858. \quad (22)$$

3.3 Accuracy assessment and cross validation

To evaluate the performance of the developed algorithm, the estimated a_g(290), S_g(250–400), and S_g(250–700) are

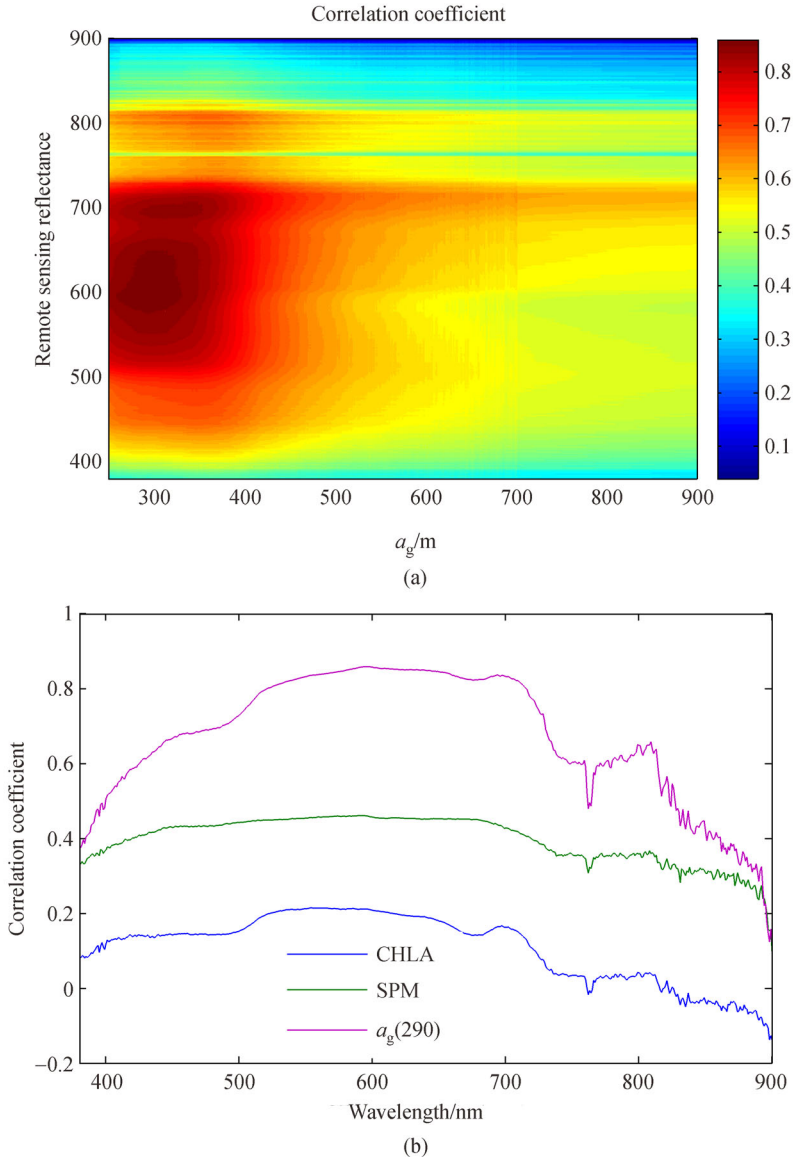

Fig. 5 (a) The color map of the correlation coefficients between the measured remote sensing reflectance (R_{rs}) at 380–900 nm and CDOM absorption (a_g) at 250–900 nm. (b) The correlation coefficients between R_{rs} at 380–900 nm and chlorophyll-a concentration (the blue line), suspended matter concentration (the green line) and $a_g(290)$ (the pink line).

compared with the *in situ* measurements in the training data set. The results are presented in Fig. 7. The retrieval of $a_g(290)$ from $R_{rs}(596)$ has a comparable accuracy with the PC1 of $R_{rs}(520–670)$, with a *MAPD* of ~32% and a *RMSE* of ~0.87 (Figs. 7(a) and 7(b)). The performance of the $R_{rs}(596)$ algorithm is slightly better than the PCA algorithm. The $S_g(250–400)$ determinations near 0.016 tend to deviate from a 1:1 relation because this S_g level corresponds to a relatively broad range of the R_{rs} gradient from 0.15 to 0.25 (Fig. 6(c)). Above 0.018, $S_g(250–400)$ is slightly underestimated, but still near the $\pm$*RMSE* line. The retrieval performance for $S_g(250–400)$ and $S_g(250–700)$ are consistent, with a *MAPD* of ~5% and a *RMSE* of ~0.0009 (Figs. 7(c) and 7(d)).

The results of the *k*-fold cross validation are presented in Table 2. An observation number (N) of 54 is used, and k is set as 6, so that each group has 9 observations. The averaged values of *MAPD* in the cross validations are ~31%, ~5.3, and ~6% for $a_g(290)$, $S_g(250–400)$, and $S_g(250–700)$, respectively, a level consistent with the assessment results for the entire data set (Fig. 7).

The a_g spectrum at 250–700 nm is then recreated based on the estimated $a_g(290)$ and $S_g(250–700)$. Figure 8 shows the *MAPD* and *RMSE* of a_g estimation at each wavelength. The *MAPD* keeps a stable level with ~30% below 450 nm. Above 450 nm, the *MAPD* rises with wavelength increase, due to the increasing uncertainties caused by the low a_g measured at longer wavelength. The *RMSE* follows an

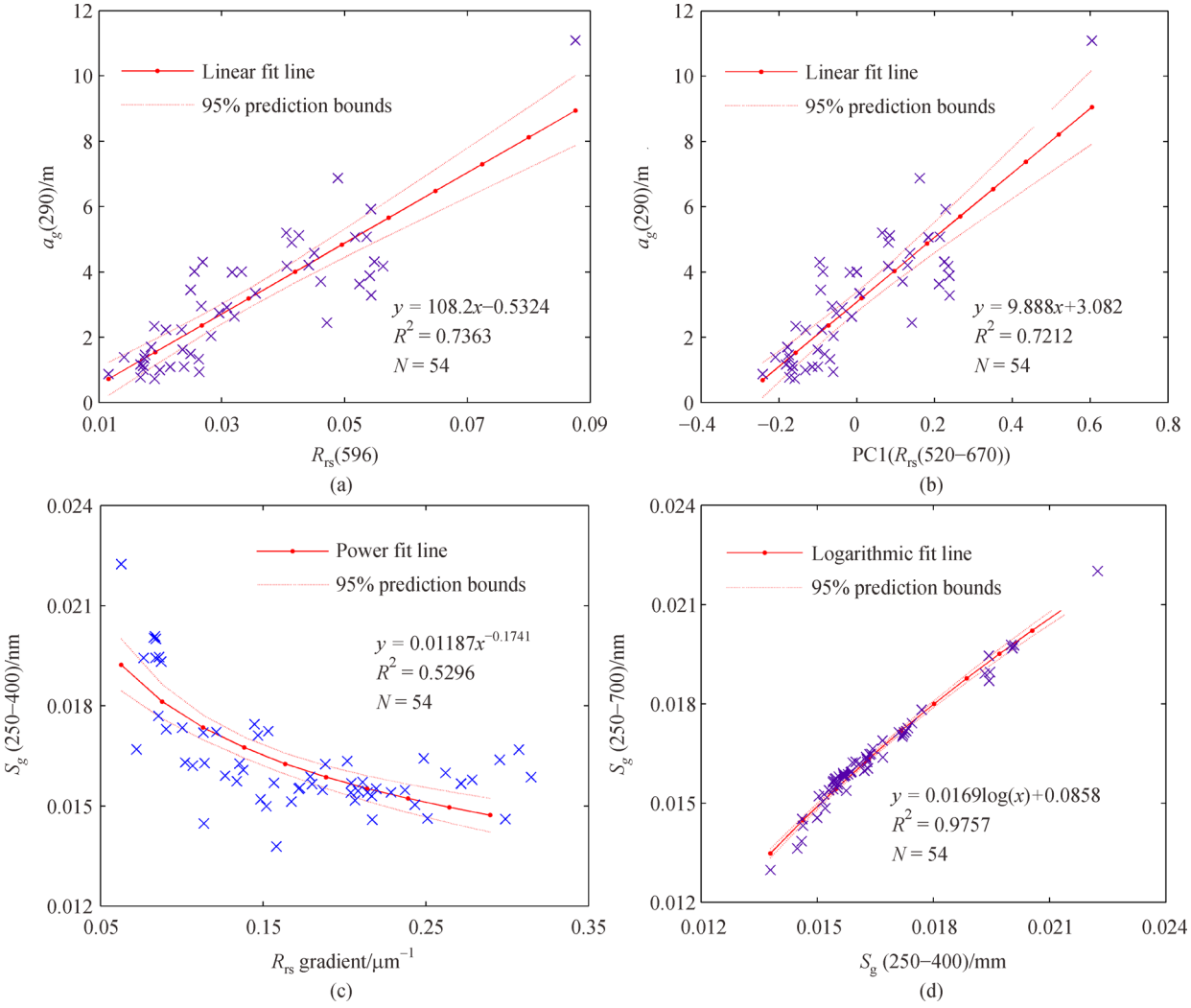

Fig. 6 Empirical relationships developed based on the *in situ* observations: the linear relationship between (a) $a_g(290)$ and $R_{rs}(596)$; (b) $a_g(290)$ and PC1(R_{rs}(520–670)); (c) the power relationship between S_g(250–400) and the R_{rs} gradient; (d) the linear relationship between S_g(250–700) and logarithm S_g(250–400). N is the number of samples in the training data set. R^2 is the determination coefficient.

exponential decrease with increasing wavelength, along with a relatively steady *MAPD*, in agreement with the shape pattern of a_g spectrum. Figure 9 shows the observations versus different estimations of a_g at 250–700 nm for all samples in the training data set. These estimations exhibit an agreement among each other. The results also demonstrate the effectiveness of our strategy to retrieve a_g and S_g in the UV range at the first step, which can avoid the influence of the low SNR of a_g measurements in the visible range.

3.4 Applications to satellite imagery

A set of satellite images acquired in spring (April and May) from 2012 to 2018 is selected for the application of the developed algorithm to match the season of the *in situ* observations in this study. For the OLI data with a 16-day revisit cycle, the time constraint is relaxed to March and June. Due to the lack of synchronous matchups of *in situ* observations and satellite data, images acquired at the same day by different sensors are chosen for cross comparison. Three pairs are finally acquired: HICO and VIIRS on 2013/04/20, OLI and VIIRS on 2016/03/26, and OLCI and VIIRS on 2017/04/02.

The $R_{rs}(596)$ algorithm is applied to derive $a_g(290)$ from the selected satellite images. Although the PCA algorithm performs well for the training data set, the values of PC1 cannot always maintain the original spatial variation pattern of reflectance when derived from satellite R_{rs}. Taking the image obtained by OLCI on 2018/04/04 as an example, Fig. 10 shows a reversed distribution pattern of PC1(R_{rs}(510–673.5)) when compared with the original pattern of R_{rs} at every single band. This may lead to unreasonable estimation of $a_g(290)$ when a linear relationship (e.g., Equation (19)) is used for CDOM absorption retrieval. In contrast, the $R_{rs}(596)$ algorithm shows higher

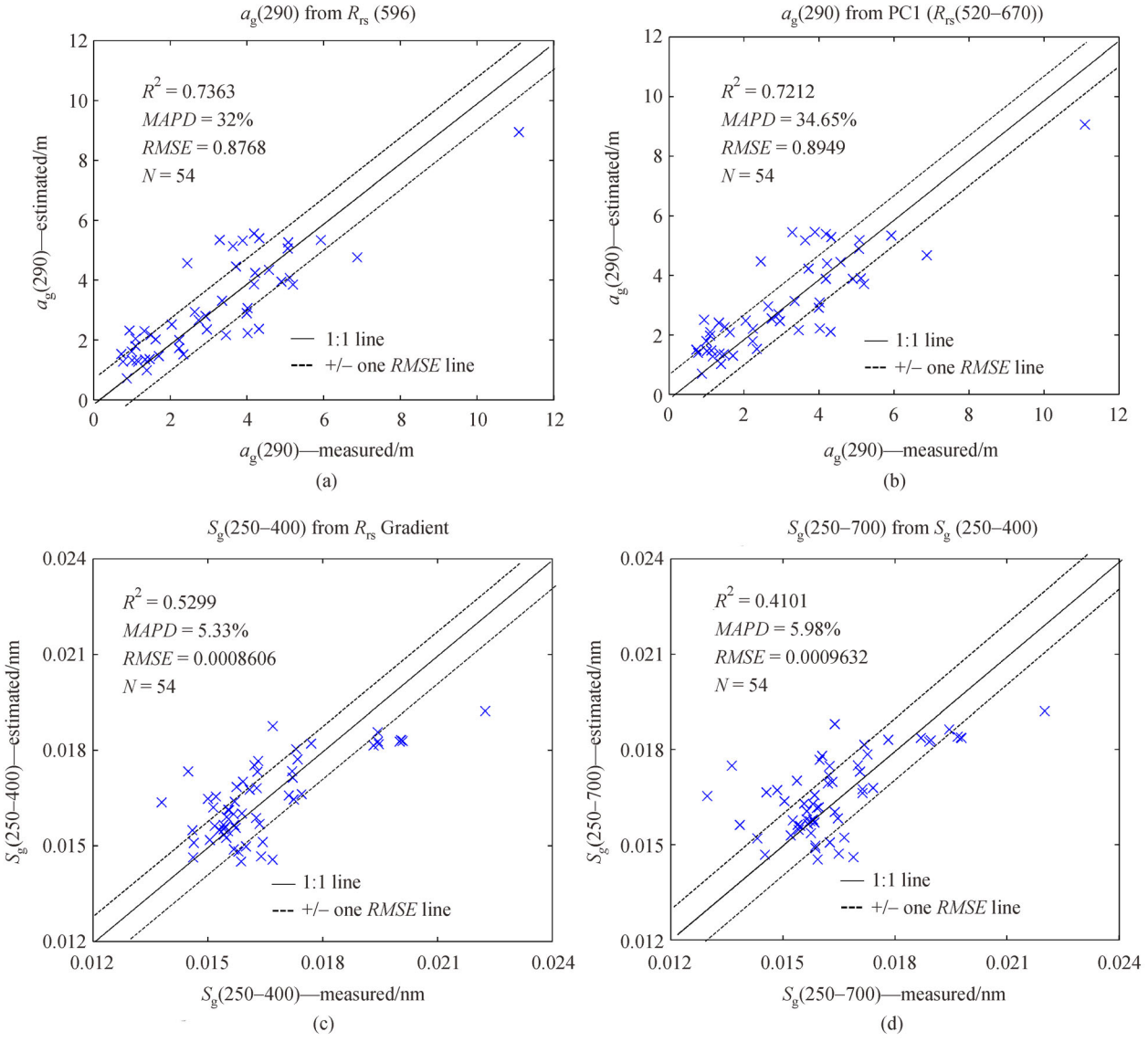

Fig. 7 Scatter plots of the observations vs. estimations of (a) $a_g(290)$ from $R_{rs}(596)$ algorithm; (b) $a_g(290)$ from PC1($R_{rs}(520–670)$) algorithm; (c) $S_g(250–400)$; and (d) $S_g(250–700)$ in the training data set. N is the number of samples. R^2 is the determination coefficient. *MAPD* is the mean absolute percentage difference; *RMSE* is the root mean square error. The solid line is 1:1 line, and the dash line is +/– one *RMSE* line from the 1:1 line.

reliability by retrieving a_g directly from the satellite R_{rs} without any statistical transforms. The $R_{rs}(596)$ is then matched to the bands of the four sensors by the criteria listed in Table 3.

When retrieving $S_g(250–400)$, the lower ends for calculation of the R_{rs} gradient (the λ_{min} in Eq. (20)) are set as 445 nm, 415.5 nm, 400 nm, and 443 nm for the VIIRS, HICO, OLCI, and OLI data, respectively, considering the available spectral range of the satellite imagery and the performance of atmospheric corrections. The range for the maximum R_{rs} is limited below 700 nm for all sensors. $S_g(250–400)$ and $S_g(250–700)$ are derived afterwards from the R_{rs} gradient by Eqs. (21) and (22).

The estimations of $a_g(290)$ and $S_g(250–400)$ from the three pairs of ocean color images are illustrated in Fig. 11 ($S_g(250–700)$ is not shown here due to little difference seen from $S_g(250–400)$). The valid range of $a_g(290)$ and $S_g(250–400)$ predicted by the developed algorithm are limited to 0–12/m and 0.012–0.024/nm, respectively (Fig. 6). Values beyond the ranges are therefore regarded as outliers and excluded from the results.

The results derived from all satellite images succeed in capturing the main distribution pattern of $a_g(290)$ and $S_g(250–400)$ shown in Figs. 3(c) and 3(d): higher $a_g(290)$ and lower $S_g(250–400)$ at the head and west side of the estuary, and a reversed pattern seen in the eastern estuary

Table 2 The results of cross validations for the four data set: $a_g(290)$ vs. $R_{rs}(596)$; $a_g(290)$ vs. PC1 ($R_{rs}(520–670)$); $S_g(250–400)$ vs. R_{rs} Gradient; and $S_g(250–700)$ vs. $S_g(250–400)$. $p1$ and $p2$ represent the coefficients in the following relationships: $a_g(290) = p1 \times R_{rs}(596) + p2$; $a_g(290) = p1 \times \text{PC1}(R_{rs}(520–670)) + p2$; $S_g(250–400) = p1 \times (R_{rs}\_\text{Gradient})^{p2}$; $S_g(250–700) = p1 \times \log(S_g(250–400)) + p2$. R^2 is the determination coefficient; *MAPD* is the mean absolute percentage difference; *RMSE* is the root mean square error

Four data set	Cross Validation	$p1$	$p2$	R^2	*MAPD*	*RMSE*
$a_g(290)$ vs. $R_{rs}(596)$	1	95.9	0.14	0.67	0.37	1.63
	2	108.8	0.44	0.76	0.44	1.03
	3	116.4	0.80	0.77	0.27	1.13
	4	106	0.56	0.73	0.17	0.87
	5	109.8	0.72	0.75	0.27	0.98
	6	111.5	0.61	0.75	0.35	0.84
	Average	**108**	**− 0.54**	**0.74**	**0.31**	**1.08**
$a_g(290)$ vs. PC1 ($R_{rs}(520–670)$)	1	8.86	3.08	0.65	0.40	1.65
	2	9.93	3.2	0.74	0.48	1.05
	3	10.62	3.08	0.75	0.28	1.11
	4	9.67	2.97	0.72	0.16	0.93
	5	10.03	2.95	0.73	0.27	0.97
	6	10.19	3.10	0.74	0.37	0.84
	Average	**9.88**	**3.06**	**0.72**	**0.33**	**1.09**
$S_g(250–400)$ vs. R_{rs} Gradient	1	0.011	0.19	0.56	0.06	0.001
	2	0.011	0.19	0.57	0.062	0.001
	3	0.012	0.14	0.44	0.077	0.0016
	4	0.012	0.17	0.51	0.016	0.0003
	5	0.012	0.18	0.55	0.045	0.0003
	6	0.012	0.18	0.54	0.04	0.0008
	Average	**0.012**	**− 0.18**	**0.53**	**0.05**	**0.0009**
$S_g(250–700)$ vs. $S_g(250–400)$	1	0.017	0.085	0.98	0.082	0.0016
	2	0.017	0.086	0.98	0.073	0.0013
	3	0.017	0.086	0.97	0.07	0.0015
	4	0.017	0.087	0.98	0.01	0.0002
	5	0.017	0.086	0.98	0.05	0.0002
	6	0.017	0.087	0.98	0.044	0.0008
	Average	**0.017**	**0.086**	**0.98**	**0.055**	**0.0009**

and near the Hong Kong coastal waters. Each pair of satellite products also show good agreements to the magnitude and distribution pattern of $a_g(290)$ and $S_g(250–400)$, demonstrating the stability and effectiveness of our algorithm among multiple sensor types. The results also reveal the influence of different spatial resolutions of satellite images on capturing variation of the CDOM absorption in the PRE with complicated hydrodynamic and biogeochemical processes. The OLI images of a spatial resolution of 30 m, the HICO images of 100 m resolution, and the OLCI images of 300 m resolution expectedly display much finer distribution patterns of $a_g(290)$ and $S_g(250–400)$ than the VIIRS images of 750 m resolution. The contrast is especially clear in the western estuary, where large amounts of terrestrial inputs mix with the estuarine water, leading to micro-scale variations of DOM concentration and diverse photochemical and biological reactions. The influence of these complicated processes is reflected in the variations of a_g and S_g, as shown in Fig. 11.

4 Discussion

The algorithm developed in this study shows promising performance in retrieving the variation of CDOM absorption in the PRE. CDOM and suspended matter dominate the optical properties of the water in the PRE during spring while phytoplankton showed little impact, and CDOM fluorescence is an important characteristic of the surface water reflectance spectrum (Mobley, 1994). A potential

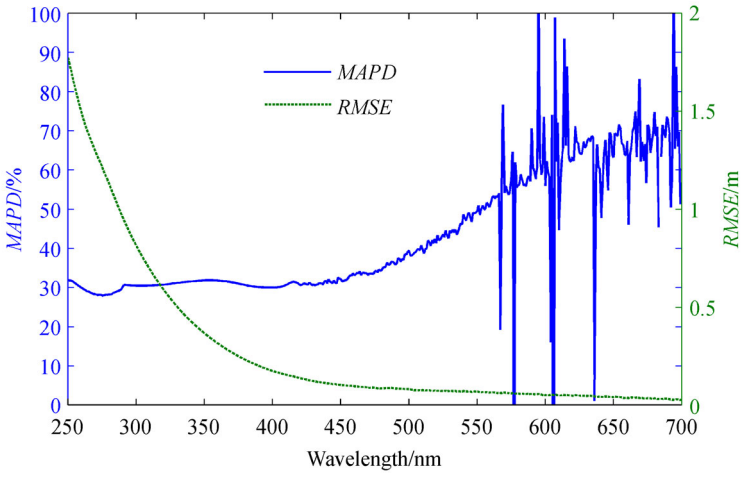

Fig. 8 *MAPD* (mean absolute percentage difference) and *RMSE* (root mean square error) of a_g estimations at each wavelength calculated based on the estimated $a_g(290)$ and $S_g(250–700)$. The line and *Y*-axis in blue represents *MAPD*, while those in green represents *RMSE*.

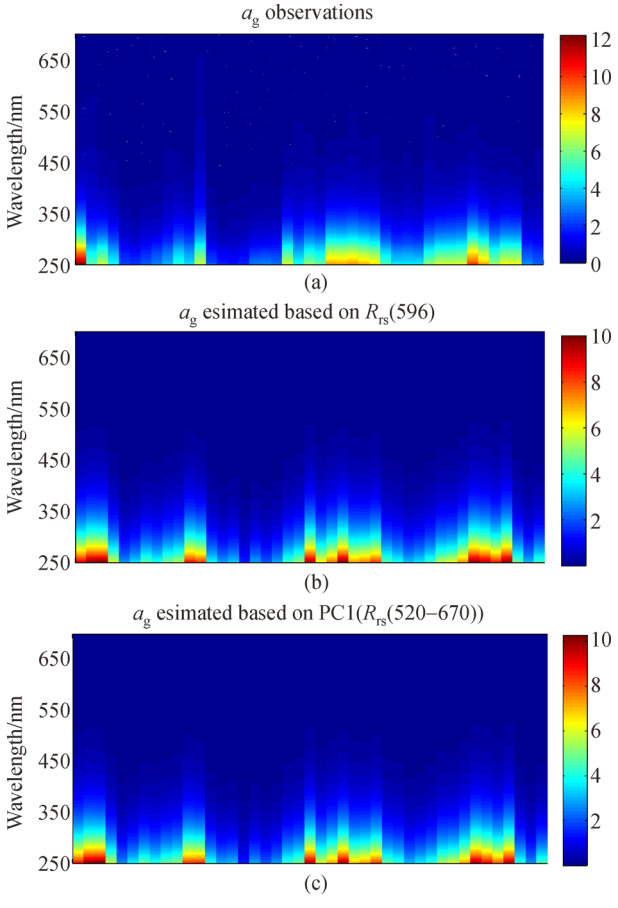

Fig. 9 Observations and estimations of a_g in 250–700 nm for all samples in the training data set: (a) a_g observations; (b) a_g estimated based on $R_{rs}(596)$ algorithm; (c) a_g estimated based on PCA algorithm. The lateral axis of these color maps represents all sampling stations in the training data set. The color bars indicate the level of CDOM absorption (in unit of m^{-1}) in the wavelength range of 250–700 nm.

connection is suggested between R_{rs} in the visible range and a_g in the UV range. This connection is further demonstrated by the strong correlations between the $R_{rs}(520–670)$ and $a_g(250–370)$, and between the R_{rs} gradient and $S_g(250–400)$ (See Fig. 5 and Section 3.2). Thus a UV scheme is developed to directly derive the CDOM UV absorption and spectral slopes from the visible reflectance. This scheme is unaffected by the interference from suspended matter, and is also able to avoid the uncertainties introduced by the low SNR of a_g in the visible range. The effectiveness of this scheme is further demonstrated by the results of algorithm evaluation and ocean color image application. Previous efforts to model the CDOM UV absorption spectra from visible remote sensing reflectance are limited due to the strong deviation of a_g(UV) from the exponential pattern for CDOM in open ocean waters (Nelson and Siegel, 2002). The deviation, however, is of an acceptable degree for coastal waters with terrestrial inputs (Cao and Miller, 2015), and, therefore does not affect the performance of our algorithm. Compared with most cases where large error is introduced by extrapolating S_g from visible to UV range (Twardowski et al., 2004), our strategy to extrapolate S_g from UV to visible range reduces this error to a large extent (see Section 3.2.3). Furthermore, previous algorithms used to derive CDOM absorption spectra generally use a uniform S_g for the entire study area to calculate a_g, which is evidently unreasonable for estuarine and coastal waters, where the CDOM of different sources may have different levels of S_g. Retrieving S_g from satellite imagery pixel by pixel using Eqs. (20)–(22) allows our algorithm to depict the variation of S_g in the PRE waters. Finally, the direct estimation of CDOM absorption from remote sensing reflectance can eliminate errors introduced by intermediate steps (Cao and Miller, 2015). Therefore our algorithm shows stable performance among various types of satellite

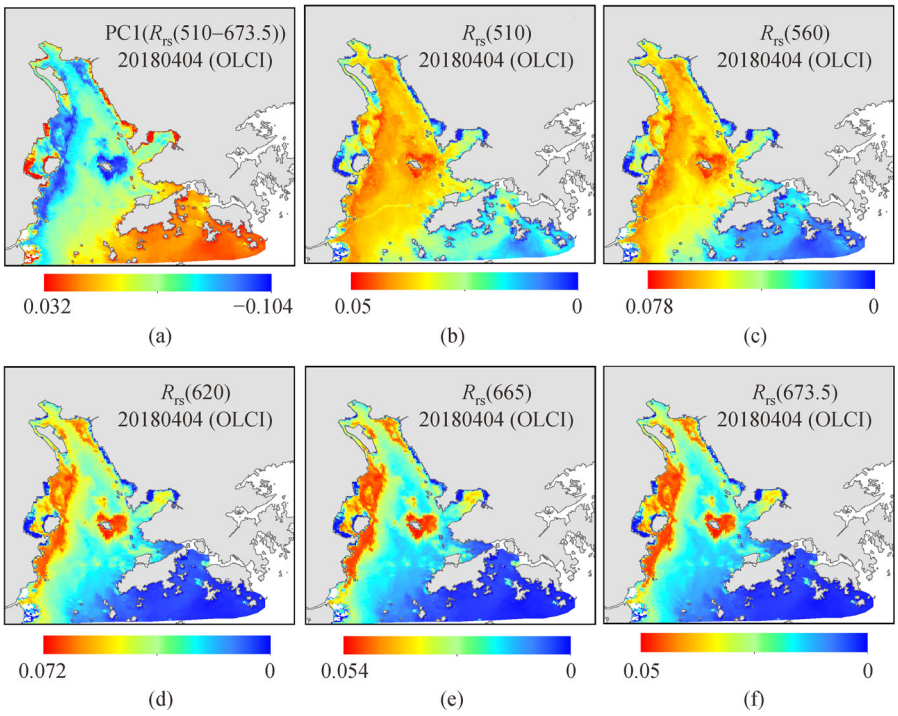

Fig. 10 Comparisons of the spatial distribution of PC1 from R_{rs}(510–673.5) and those of R_{rs}(510), R_{rs}(560), R_{rs}(620), R_{rs}(665), and R_{rs}(673.5) obtained by OLCI on 2018/04/04 in the Pearl River Estuary.

Table 3 The criterion used to match R_{rs}(596) with the bands of four sensors. For VIIRS, R_{rs}(596) is calculated by the weighted average of B(555) and B(672). For OLCI and HICO, R_{rs}(596) is calculated by the average of B(560) and B(620), B(593) and B(599), respectively. For OLI, value of B3 (526–600) is directly adopted as R_{rs}(596).

Sensor	Spectral bands in visible range/nm	R_{rs}(596)
VIIRS	412/445/488/555/672	[0.66B(555) + 0.34B(672)]/2
OLCI	400/412.5/442.5/490/510/560/620/665/673.75/681.25	[B(560) + B(620)]/2
HICO	4047–696 (52 bands with interval of ~5.7 nm)	[B(593) + B(599)]/2
OLI	433–453/450–515/525–600/630–680	B3 (525–600)

images with different spatial and spectral resolutions, with a distinctive advantage in capturing multi-scaled features related to diverse hydrodynamic and biogeochemical processes in estuaries and coastal waters.

There are certain limitations to our methodology. First, the algorithm is empirically developed based on a spring observational cruise in the Pearl River Estuary during the wet season when fresh water discharge from upper stream can reach the annual peak. Large amounts of terrestrial inputs render CDOM and suspended matter instead of phytoplankton to be the predominant optical constituents. In the dry season (autumn and winter), the situation may change and the algorithm may no longer be applicable. For example, according to the Report on the Marine Environmental Quality in Guangdong (Administration of Ocean and Fisheries of Guangdong Province, 2013–2016), several algal blooms reported in the PRE in recent years all occurred from November to February, suggesting that chlorophyll concentration may accumulate during the dry season. As a result, the spectral curve of reflectance may be altered accordingly. The *in situ* measured R_{rs} in spring showed only one peak near 580 nm (partially attributed to CDOM absorption), hence, our algorithm may be unsuitable for other types of R_{rs} that exhibit peaks and valleys at different wavelengths relative to other colored components. Second, since CDOM absorption is directly derived from remote sensing reflectance, the estimations are highly sensitive to the cumulative uncertainties associated with the R_{rs} signal at the different bands considered (Vantrepotte et al., 2015). The visible blue band is particularly notable, as the current atmospheric correction methodology tends to overcorrect aerosol effects at the blue bands, especially for coastal zones, resulting in large errors and even negative values of R_{rs} in this range (Siegel et al., 2000; Cao and Miller, 2015). To reduce such errors, the data quality of R_{rs} at the blue bands by different sensors is carefully examined when determining the lower end for R_{rs} gradient calculation in this work. Third, the application

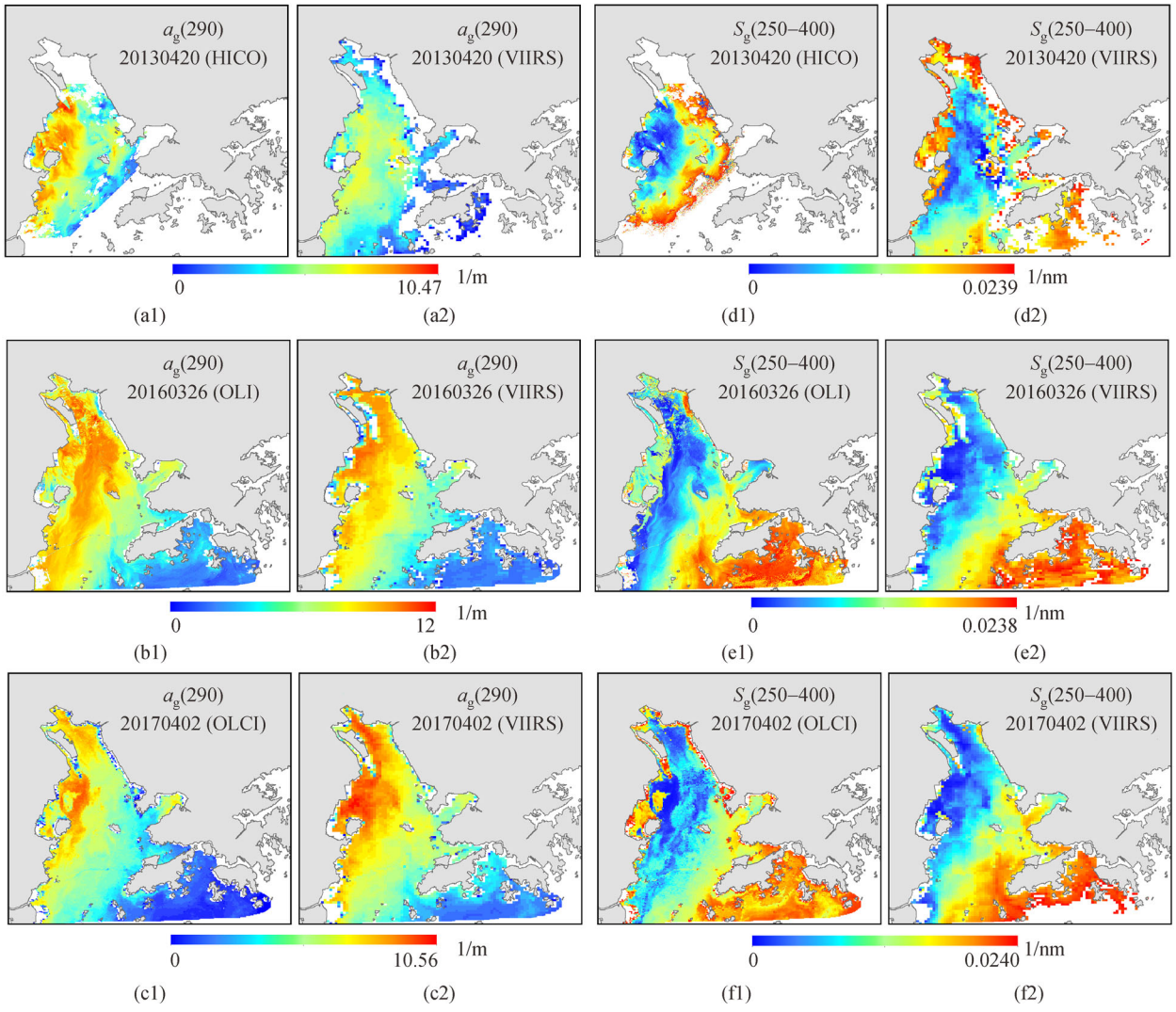

Fig. 11 Estimations of $a_g(290)$ and $S_g(250–400)$ for three pairs of ocean color images: HICO and VIIRS on 2013/04/20, OLI and VIIRS on 2016/03/26, and OLCI and VIIRS on 2017/04/02.

of the PCA algorithm (Eq. (19)) to satellite imagery should be further examined in quantitative remote sensing. While R_{rs} has a clear physical meaning, the principal components obtained from PCA are a set of projections whose variations are no longer a direct reflection of the characteristics of the original physical space. Even though a good correlation is shown between PC1 and $a_g(290)$ in the training data set, the relationship may be false in ocean color applications. This is probably because the nature of a discrete sampling space may differ from that of a continuous imaging space.

5 Conclusions

This study has developed a UV to visible scheme to retrieve CDOM absorption from remote sensing reflectance based on a set of observations in the Pearl River Estuary in spring. The scheme is free from the interference of suspended matter and the effect of uncertainties produced by low SNR a_g in visible range. Our algorithm shows good performance in estimating CDOM absorption and spectral slopes with the *MAPD* of a_g in 250–450 nm, $S_g(250–400)$, and $S_g(250–700)$ nm being ~30%, ~5%, and ~6%, respectively. The algorithm also successfully captures the distribution pattern of CDOM absorption in the PRE waters from satellite imagery with multiple spatial and spectral resolutions. The UV-visible scheme can be easily applied to similar Case-2 waters using new data set and calibrated fitting coefficients, therefore our algorithm provides an effective approach to address CDOM variations in Case-2 waters where terrestrial inputs are significant, and CDOM and suspended matter dominate the water optical properties instead of phytoplankton. The algorithm is also capable of retrieving

a_g and S_g from satellite ocean color imagery at high spatial resolution, which can reveal micro-scaled features of diverse hydrodynamic and biogeochemical processes in estuaries and coastal waters, and particularly benefits quantitative remote sensing studies for water regions with complicated circulations and abundant chemical and biological activities.

Acknowledgements This work was supported by the National Natural Science Foundation of China (Grant No. 41376035), the General Research Fund of Hong Kong Research Grants Council (RGC) (Nos. CUHK 14303818, 402912, and 403113), the Hong Kong Innovation and Technology Fund (Nos. ITS/259/12 and ITS/321/13).

References

Administration of Ocean and Fisheries of Guangdong Province (2013–2016). Report on the Marine Environmental Quality in Guangdong. Available at Guangdong Government website

Blough N V, Del Vecchio R (2002). Chromophoric dissolved organic matter (CDOM) in the coastal environment. In: Hansell D, Carlson C, eds. Biogeochemistry of Marine Dissolved Organic Matter. San Diego, CA: Academic Press, 509–546

Bricaud A, Morel A, Prieur L (1981). Absorption by dissolved organic matter of the sea (yellow substance) in the UV and visible domains. Limnol Oceanogr, 26(1): 43–53

Callahan J, Dai M H, Chen R F, Li X L, Lu Z M, Huang W (2004). Dissolved organic matter in the Pearl River Estuary, China. Mar Chem, 89(1-4): 211–224

Cao F, Miller W L (2015). A new algorithm to retrieve chromophoric dissolved organic matter (CDOM) absorption spectra in the UV from ocean color. J Geophys Res Oceans, 120(1): 496–516

Carder K L, Steward R G (1985). A remote-sensing reflectance model for a red tide dinoflagellate off West Florida. Limnol Oceanogr, 30 (2): 286–298

Chen C Q, Shi P, Yin K D, Pan Z L, Zhan H G, Hu C M (2003). Absorption coefficient of yellow substance in the Pearl River Estuary. In: Proceedings of Ocean Remote Sensing and Applications. Bellingham WA: SPIE, 4892: 215–221

Chen Z, Li Y, Pan J (2004). The distributions of the optical properties of colored dissolved organic matter and dissolved organic carbon in the Pearl River Estuary. Cont Shelf Res, 24: 1845–1856

Church M J, Ducklow H W, Karl D M (2002). Multi-year increases in dissolved organic matter inventories at Station ALOHA in the North Pacific Subtropical Gyre. Limnol Oceanogr, 47(1): 1–10

Deng Z, He Q, Yang Q, Lin J (2015). Observations of *in situ* flocs characteristics in the Modaomen Estuary of the Pearl River. Haiyang Xuebao, 37(9): 152–161 (in Chinese)

Ducklow H W (2002). Forword. In: Hansell D, Carlson C, eds. Biogeochemistry of Marine Dissolved Organic Matter. San Diego, CA: Academic Press

Fichot C G, Benner R (2012). The spectral slope coefficient of chromophoric dissolved organic matter (S275–295) as a tracer of terrigenous dissolved organic carbon in river-influenced ocean margins. Limnol Oceanogr, 57(5): 1453–1466

Fichot C G, Benner R, Kaiser K, Shen Y, Amon R M W, Ogawa H, Lu C J (2016). Predicting dissolved lignin phenol concentrations in the coastal ocean from chromophoric dissolved organic matter (CDOM) absorption coefficients. Front Mar Sci, 3(7): 1–15

Fu D, Luan H, Liu D, Zhang Y, Ding Y, Wang W, Li X, Jiang C (2016). Analysis of suspended sediment concentration remote sensing models in winter and spring in the Pearl River estuary. Haiyang Huanjiang Kexue, 35(4): 600–604 (in Chinese)

Geisser S (1993). Predictive Inference. New York, NY: Chapman and Hall

Gordon H R, Wang M (1994). Retrieval of water-leaving radiance and aerosol optical thickness over the oceans with SeaWiFS: a preliminary algorithm. Appl Opt, 33(3): 443–452

Helms J R, Stubbins A, Perdue E M, Green N W, Chen H, Mopper K (2013). Photochemical bleaching of oceanic dissolved organic matter and its effect on absorption spectral slope and fluorescence. Mar Chem, 155: 81–91

Helms J R, Stubbins A, Ritchie J D, Minor E C, Kieber D J, Mopper K (2008). Absorption spectral slopes and slope ratios as indicators of molecular weight, source, and photobleaching of chromophoric dissolved organic matter. Limnol Oceanogr, 53(3): 955–969

Hong H S, Wu J Y, Shang S L, Hu C M (2005). Absorption and fluorescence of chromophoric dissolved organic matter in the Pearl River Estuary, South China. Marine. Chemistry, 97: 78–89

IOCCG (2016). Remote sensing of inherent optical properties: Fundamentals, tests of algorithms, and applications. In: Lee Z P, ed. Reports of the International Ocean-Colour Coordinating Group (No. 5). Dartmouth, Canada: IOCCG

Laane R W P M, Kramer K J M (1990). Natural fluorescence in the North Sea and its major estuaries. Neth J Sea Res, 26(1): 1–9

Lee Z, Carder K L, Hawes S K, Steward R G, Peacock T G, Davis C O (1994). Model for the interpretation of hyperspectral remote-sensing reflectance. Appl Opt, 33(24): 5721–5732

Lei X, Pan J Y, Devlin A T (2018). Mixing behavior of chromophoric dissolved organic matter in the Pearl River Estuary in spring. Cont Shelf Res, 154: 46–54

Liu D, Zhang C, Fu D, Shen C (2010). Hyperspectral data-based remote-sensing inversion model for suspended sediment in surface waters at the Pearl River Estuary. Mark Sci, 34(7): 77–80 (in Chinese)

Liu F, Chen C, Tang S, Liu D (2009). A piecewise algorithm for retrieval of suspended sediment concentration based on *in situ* spectral data by MERIS in Zhujiang River Estuary. Journal of Tropical Oceanography, 28(1): 9–14 (in Chinese)

Loisel H, Morel A (2001). Non-isotropy of the upward radiance field in typical coastal (Case 2) waters. Int J Remote Sens, 22(2–3): 275–295

Loiselle S A, Bracchini L A, Dattilo M, Ricci M, Tognazzi A, Cózar A, Rossi C (2009). Optical characterization of chromophoric dissolved organic matter using wavelength distribution of absorption spectral slopes. Limnol Oceanogr, 54(2): 590–597

Loiselle S, Vione D, Minero C, Maurino V, Tognazzi A, Dattilo A M, Rossi C, Bracchini L (2012). Chemical and optical phototransformation of dissolved organic matter. Water Res, 46(10): 3197–3207

Mobley C (1994). Light and water: radiative transfer in natural waters. New York: Academic Press

Mobley C D (1999). Estimation of the remote-sensing reflectance from above-surface measurements. Appl Opt, 38(36): 7442–7455

Morel A, Gentili B (1993). Diffuse reflectance of oceanic waters. II

Bidirectional aspects. Appl Opt, 32(33): 6864–6879

Morel A, Mueller J L (2002). Normalized water-leaving radiance and remote sensing reflectance. Bidirectional reflectance and other factors. In: Ocean Optics Protocols for Satellite Ocean Color Sensor Validation (Revision. 4). NASA: 3: 32–59

Morel A, Prieur L (1977). Analysis of variations in ocean color. Limnol Oceanogr, 22(4): 709–722

Mueller J L, Davis C, Arnone R, Frouin R, Carder K, Lee Z P, Steward R G, Hooker S, Mobley C D, Mclean S (2002). Above-water radiance and remote sensing reflectance measurement and analysis protocols. In: Ocean Optics Protocols for Satellite Ocean Color Sensor Validation (Revesion 4). NASA: 3: 21–31

NASA Goddard Space Flight Center, Ocean Ecology Laboratory, Ocean Biology Processing Group (2018). Ocean and Land Colour Imager (OLCI) L1 Data; NASA OB.DAAC, Greenbelt, MD, USA

Nelson N B, Siegel D A (2002). Chromophoric dissolved organic matter (CDOM) in the open ocean. In Hansell D, Carlson C, eds. Biogeochemistry of Marine Dissolved Organic Matter. San Diego, CA: Academic Press, 547–578.

Pan J Y, Gu Y Z (2016). Cruise observation and numerical modeling of turbulent mixing in the Pearl River estuary in summer. Cont Shelf Res, 120: 122–138

Sharpless C M, Blough N V (2014). The importance of charge-transfer interactions in determining chromophoric dissolved organic matter (CDOM) optical and photochemical properties. Environ Sci Process Impacts, 16(4): 654–671

Siegel D A, Maritorena S, Nelson N B, Hansell D A, Lorenzi-Kayser M (2002). Global distribution and dynamics of colored dissolved and detrital organic materials. J Geophys Res, 107(C12): 3228–3242

Siegel D A, Wang M, Maritorena S, Robinson W (2000). Atmospheric correction of satellite ocean color imagery: the black pixel assumption. Appl Opt, 39(21): 3582–3591

Stedmon C A, Markager S (2001). The optics of chromophoric dissolved organic matter (CDOM) in the Greenland Sea: an algorithm for differentiation between marine and terrestrially derived organic matter. Limnol Oceanogr, 46(8): 2087–2093

Stedmon C A, Nelson N B (2015). The optical properties of DOM in the ocean. In: Hansell D, Carlson C, eds. Biogeochemistry of Marine Dissolved Organic Matter. 2nd ed. San Diego, CA: Academic Press, 481–508

Twardowski M S, Boss E, Sullivan J M, Donaghay P L (2004). Modeling the spectral shape of absorption by chromophoric dissolved organic matter. Mar Chem, 89(1–4): 69–88

Vantrepotte V, Danhiez F P, Loisel H, Ouillon S, Mériaux X, Cauvin A, Dessailly D (2015). CDOM-DOC relationship in contrasted coastal waters: implication for DOC retrieval from ocean color remote sensing observation. Opt Express, 23(1): 33–54

Vermote E (2016). VNP09-VIIRS/NPP Atmospherically Corrected Surface Reflectance 6-Min L2 Swath IP 375m, 750m, NASA Level-1 and Atmosphere Archive & Distribution System (LAADS) Distributed Active Archive Center (DAAC). Goddard Space Flight Center, Greenbelt, MD

Wang G, Cao W, Xu D, Yang D (2007). Variations in the light absorption coefficients of non-algal particels in the north of the South China Sea. HAIYANG JISHU, 26(1): 45–53 (in Chinese)

Wang S S, Wang Y B, Fu Q H, Yin B, Li Y M (2014). Spectral absorption properties of the water constituents in the estuary of Zhujiang River. Environm Sci, 35(12): 4511–4521 (in Chinese)

Wei J, Lee Z, Ondrusek M, Mannino A, Tzortziou M, Armstrong R (2016). Spectral slopes of the absorption coefficient of colored dissolved and detrital material inverted from UV-visible remote sensing reflectance. J Geophys Res Oceans, 121(3): 1953–1969

Xu X, Cao W, Yang Y (2004). Relationships between spectral absorption coefficient of particulates and salinity and chlorophyll a concentration in Zhujiang River mouth. J Tropical Oceanogra, 23(5): 63–71 (in Chinese)

Yang J, Chen C (2007). An optimal algorithm for retrieval of chlorophyll, suspended sediments and gelbstoff of case II waters in Zhujiang River estuary. J Tropical Oceanogra, 26(5): 15–20 (in Chinese)

Zhou H, Han B, Li T, Zhu J, Wang X (2007). Variations in the light absorption coefficients of de-pigment par ticles in South Yellow Sea and Zhu Jiang Kou of China. Ocean Technology, 26(3): 114–117 (in Chinese)

AUTHORS BIOGRAPHIES

Xia Lei was born in Shanxi, China, in 1988. She received the B.S. degree in geomatics from Jilin University, China in 2010, and the M. S. degree in signal processing from University of Chinese Academy of Sciences, China in 2013, and is currently pursuing the Ph.D. degree in earth system and geoinformation science at the Chinese University of Hong Kong, Hong Kong. From 2013 to 2015, she was a Research Assistant with the State Key laboratory of Remote Sensing Science, Chinese Academy of Sciences. Her research interests include the optical properties of natural waters and ocean color remote sensing. E-mail: 1155074880@link.cuhk.edu.hk.

Pan J received the M.Sc. degree in optics from the Chinese Academy of Sciences (CAS), Hefei, China, in 1988 and the Ph.D. degree in physical oceanography from CAS, Qingdao, China, in 1996. He was with the University of Delaware, Newark, DE, USA; The University of Southern Mississippi, Stennis Space Center, MS, USA; Oregon Health and Science University, Portland, OR, USA; and Portland State University, Portland. Since 2009, he has been with the Institute of Space and Earth Information Science, The Chinese University of Hong Kong, Shatin, Hong Kong. His study interests include marine remote sensing, coastal oceanography, river plume dynamics, etc. E-mail: panj@cuhk.edu.hk.

Adam T Devlin was born in Chicago, IL, USA, in 1977. He received the B.S. degree from the University of Oregon, Eugene, OR, USA, in 2001, the M.S. degree in applied physics from Appalachian State University, Boone, NC, USA, in 2003, and the Ph.D. degree in applied physics from Portland State University, Portland, OR, in 2016. He is a Postdoctoral Fellow with The Chinese University of Hong Kong, Shatin, Hong Kong. His research interests involve physical oceanography, climate analysis, and remote sensing of geophysical and oceanic variability and his main focus is on ocean tides and sea level variability. E-mail: phlux1@gmail.com.